Stochastic Medial Axis Transform for Bayesian Extended Object Tracking

Jiachen Zhou and **Uwe D. Hanebeck**
Intelligent Sensor-Actuator-Systems Laboratory (ISAS)
Institute for Anthropomatics and Robotics
Karlsruhe Institute of Technology (KIT), Germany
jiachen.zhou@kit.edu, uwe.hanebeck@kit.edu

Albert Bauer and **Harald Kruggel-Emden**
Chair of Mechanical Process Engineering and Solids Processing
Institute of Chemical and Process Engineering
Technische Universität Berlin (TUB), Germany
a.bauer@tu-berlin.de, kruggel-emden@tu-berlin.de

***Abstract*—In this paper, we present novel results and insights into tracking extended objects using the Stochastic Medial Axis Transform (SMAT). Unlike conventional methods that depend on explicit shape parameterization with basic priors, SMAT employs an implicit inside-out representation by constructing maximum inscribed circles within the object. This is achieved by simultaneously fitting two Bézier curves: one that defines the medial manifold, providing the centers of the maximum inscribed circles, and the other that characterizes the scalar thickness field, assigning positive radii to these centers. This dual-curve formulation leverages the concept of inverse skeletonization and offers a flexible, parametric shape model capable of tracking diverse shapes, whether convex or non-convex, symmetric or asymmetric. Furthermore, we obtain a closed-form likelihood function in 2D space that facilitates the application of advanced recursive Bayesian state estimators. Finally, we conduct two simulation studies to demonstrate and evaluate the effectiveness of the proposed approach.**

***Index Terms*—Extended object tracking, Stochastic Medial Axis Transform, Bayesian inference, nonlinear filtering, Gaussian assumed density filter, measurement association problem**

I. INTRODUCTION

A. Context

We consider the problem of extended object tracking (EOT), where the main objective is to simultaneously estimate the target's kinematic state and its spatial extent (or shape) recursively over time, using noisy position measurements obtained from the target's surface. While EOT is widespread in autonomous navigation, it is equally critical for advancing particle measurement techniques. Accurate shape reconstruction of particulate solids is essential, as morphology directly affects their behavior in industrial processes. Integrated with novel tracking methods, this combination enables significant gains in measurement accuracy across diverse particulate applications.

Recent advances in sensor resolution and multi-modal integration have dramatically increased the quantity and quality of tracking data, which benefits EOT, where targets are modeled by their spatial extent rather than as points. These rich measurements enable a more accurate joint estimation of both the object's pose and its shape via probabilistic nonlinear filtering. In this framework, the system state includes the object's position, orientation, shape parameters, and optionally velocities or accelerations. Since the system state is usually not directly observable, it must be inferred from measurement data. Thus, a key objective of EOT is to effectively interpret and process position measurements using a reasonable measurement model.

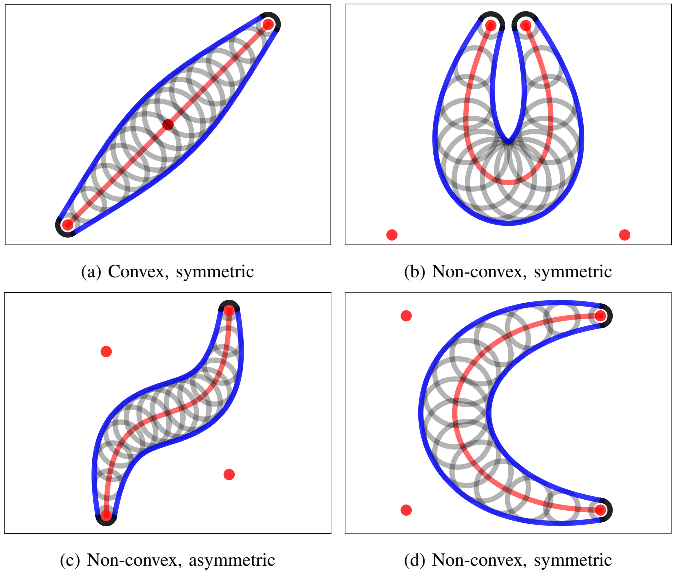
(a) Convex, symmetric
(b) Non-convex, symmetric
(c) Non-convex, asymmetric
(d) Non-convex, symmetric

Fig. 1: Illustration of diverse shapes generated by the presented method. A Bézier curve, parameterized by its control points (red dots), defines the medial axis (red solid line) within the target, thereby establishing the centers of all maximum inscribed circles (gray). A second Bézier curve specifies the scalar thickness field, assigning radii to these centers. Consequently, envelopes (blue) that enclose all maximum inscribed circles are derived to approximate the target shape, with the envelope boundaries completed by two solid black lines.

B. State of the Art

Prior to defining a measurement model, it is essential to establish the spectrum of shape models. The complexity of these models is governed by both the richness of the measurement data and the amount of prior knowledge available, ranging from basic, robust approximations to highly detailed, flexible reconstructions. When the target is a priori assumed to have a simple shape, elementary geometric models such as lines [1] or rectangles [2] are commonly used and can still yield robust tracking, even with sparse surface measurements. Among parametric models, ellipses are particularly widespread in high-noise scenarios, supported by the analytical framework of Random Matrix (RM) theory [3], [4]. For lower noise environments, more expressive models like the Random Hypersurface Model (RHM) [5], [6] are feasible, where measurements are assumed to stem from a randomly scaled version of the target boundary. For complex, irregular, or non-convex targets that cannot be captured by simple parameterizations, more flexible shape models become essential. Examples include parametric radial representations based on Fourier series [7] and non-parametric approaches using Gaussian processes [8].

EOT is typically formulated as a nonlinear state estimation problem solved via recursive Bayesian filtering. However, the resulting state probability density functions (PDFs) are often multi-modal or non-Gaussian, making closed-form solutions infeasible. Therefore, simplifications are introduced in the form of Gaussian Assumed Density Filters (GADFs), which approximate the true complex state PDF as a single Gaussian after each processing step. Various Nonlinear Kalman Filters (NKFs), including the Unscented Kalman Filter (UKF) [9] and the Smart Sampling Kalman Filter (S^2KF) [10], [11], have been employed to track targets modeled by star-convex RHMs [7]. During each measurement update, they linearize the nonlinear measurement equation and then apply Kalman Filter formulas. Nevertheless, in the presence of strong nonlinearity, these filters exhibit reduced estimation accuracy due to large linearization errors. Alternatively, particle flow-based Progressive Gaussian Filters (PGFs) [12], [13] avoid such linearization by a progression mechanism, which decomposes each measurement update into successive sub-updates and gradually integrates measurement information into state estimates. A closed-form likelihood function for target tracking has been derived by leveraging the PGF framework [14].

A closely related approach is spline-based tracking of curved extended targets [15]. Here, the target is modeled as a "thick" Bézier curve with non-zero width and is approximated by a rectangle chain. While this method allows for modeling of both convex and non-convex shapes, approximation of a continuous boundary with a set of discrete rectangles may introduce modeling errors. Moreover, the computational complexity may rise as the number of rectangles increases, particularly when capturing highly irregular target deformations.

C. Contributions

In this work, we introduce Stochastic Medial Axis Transform (SMAT), an innovative extension of the long-established MAT theory. Our key novelty is to transform the traditionally intractable computation of an object's exact medial representation into a stochastic state estimation problem, thereby making it inherently tractable. To realize this reformulation in practice, we introduce a tailored dynamic system, where all parameters necessary for constructing the SMAT are recursively estimated over time. Notably, such a treatment has rarely been discussed and remains unexplored.

Although rooted in MAT theory, our novel method deviates significantly from existing MAT algorithms, which primarily aim to approximate the exact internal medial axis and lack analytical solutions [16], [17]. Instead, we leverage our estimated SMAT model to reconstruct a smooth boundary of an unknown object. Rather than relying on predefined shape assumptions through, e.g., parameterizing explicit basic shape priors or combining multiple parametric models, SMAT employs a flexible, parametric shape model, specifically tailored for EOT. This strategy effectively tracks a wide range of shapes, whether convex or non-convex, symmetric or asymmetric.

More precisely, we adopt a synthetic medial representation by constructing maximum inscribed circles within the target of interest. This is achieved by simultaneously defining and parameterizing two Bézier curves: one modeling a continuous medial manifold that provides the centers of the largest circles, and the other representing a continuous scalar thickness field that assigns corresponding positive radii to these centers. Moreover, by adjusting the control points of both curves, non-rigid deformations such as bending and compression are effectively captured. In this dual-curve formulation, the target's boundary is implicitly reconstructed by the envelope of all the maximum inscribed circles from the inside out with arbitrary flexibility. Based on this shape model design, a closed-form likelihood function is derived, enabling the application of advanced recursive Bayesian estimators for nonlinear filtering.

II. PROBLEM FORMULATION

Our goal is to estimate an unknown extended object's parameters, in particular its shape, position, and orientation, based on noisy position measurements collected from its surface in a two-dimensional plane. At time step k, the system state $\underline{\boldsymbol{x}}_k$, which encapsulates all necessary kinematic and extent parameters, is denoted by

$$\underline{\boldsymbol{x}}_k = \left[(\underline{\boldsymbol{x}}_k^{\text{kin.}})^\top ,\ (\underline{\boldsymbol{x}}_k^{\text{ext.}})^\top \right]^\top \ . \tag{1}$$

The kinematic state $\underline{\boldsymbol{x}}_k^{\text{kin.}}$ typically consists of the target's position, velocity magnitude, heading angle and turn rate. The random vector $\underline{\boldsymbol{x}}_k^{\text{ext.}}$ represents the parameters of the target shape and will be discussed in Section IV.

During each measurement update, we assume the availability of a measurement set $\mathcal{Y}_k = \{\tilde{\underline{y}}_{k,i}\}_{i=1}^{N_k}$, consisting of N_k individual position measurements in Cartesian coordinates. The total number of measurements N_k can vary over time. These measurements are highly informative to infer the hidden system state, as they not only provide evidence about the target's kinematic state, but also reflect characteristics of its spatial extent. Each individual measurement $\tilde{\underline{y}}_{k,i}$ is modeled as a noisy observation of an unknown two-dimensional point $\underline{\boldsymbol{z}}_{k,i}^{\boldsymbol{x}}$, referred to as the measurement source, which is assumed to lie on the target boundary, i.e.,

$$\tilde{\underline{y}}_{k,i} = \underline{\boldsymbol{z}}_{k,i}^{\boldsymbol{x}} + \underline{\boldsymbol{v}}_{k,i} \ , \ i = 1, \ldots, N_k \ , \tag{2}$$

where $\underline{\boldsymbol{v}}_{k,i}$ denotes additive zero-mean Gaussian white noise with a known probability distribution. Noise terms for different measurements are mutually independent and also independent of the state.

We denote the PDF of the state $\underline{\boldsymbol{x}}_k$ at time step k conditioned on the k received measurement sets $\mathcal{Y}_1, \ldots, \mathcal{Y}_k$ as

$$f_{\boldsymbol{x}_k}^{e}(\underline{x}_k) = f_{\boldsymbol{x}_k}\left(\underline{x}_k \mid \mathcal{Y}_1, \ldots, \mathcal{Y}_k\right) = f_{\boldsymbol{x}_k}\left(\underline{x}_k \mid \mathcal{Y}_{1:k}\right) \ , \tag{3}$$

and the predicted state density, namely the state PDF at time step k conditioned only on $\mathcal{Y}_1, \ldots, \mathcal{Y}_{k-1}$ as

$$f^{p}_{\boldsymbol{x}_k}(\underline{x}_k) = f_{\boldsymbol{x}_k}\left(\underline{x}_k \mid \mathcal{Y}_{1:k-1}\right) \ . \tag{4}$$

One of our primary objectives is to correct the predicted state estimate $f^{p}_{\boldsymbol{x}_k}(\underline{x}_k)$ using the newly arrived measurements $\mathcal{Y}_k = \{\tilde{\underline{y}}_{k,i}\}_{i=1}^{N_k}$. Typically, this refinement is performed by applying Bayes' rule and assuming that the current measurement set $\mathcal{Y}_k$ is conditionally independent of the already processed measurement sets $\mathcal{Y}_{1:k-1}$ given the predicted state estimate

$$f\left(\mathcal{Y}_k \mid \underline{x}_k,\, \mathcal{Y}_{1:k-1}\right) = f\left(\mathcal{Y}_k \mid \underline{x}_k\right) \ . \tag{5}$$

The corrected state density then follows as

$$f^{e}_{\boldsymbol{x}_k}(\underline{x}_k) \propto f(\mathcal{Y}_k \mid \underline{x}_k)\; f^{p}_{\boldsymbol{x}_k}(\underline{x}_k) \ . \tag{6}$$

By exploiting the mutual independence of the noise terms, we obtain a likelihood function that simultaneously processes all the measurements within a single filter step

$$f(\mathcal{Y}_k \mid \underline{x}_k) = \prod_{i=1}^{N_k} f_{\boldsymbol{y}_k}(\tilde{\underline{y}}_{k,i} \mid \underline{x}_k) \ . \tag{7}$$

A key benefit of this factorization is that each measurement $\tilde{\underline{y}}_{k,i}$ can be processed independently. First, we express the generative measurement model (2) in probabilistic form as the conditional density $f_{\boldsymbol{y}_k}(\underline{y}_{k,i} \mid\, \underline{x}_k)$. We then define the likelihood function for a specific observation $\tilde{\underline{y}}_{k,i}$ as $f^{\mathrm{L}}_{k,i}(\underline{x}_k) \overset{\text{def}}{=} f_{\boldsymbol{y}_k}(\tilde{\underline{y}}_{k,i} \mid \underline{x}_k)$. Once this likelihood function $f^{\mathrm{L}}_{k,i}(\underline{x}_k)$ is explicitly obtained, it can be incorporated into a recursive Bayesian filter for extended object tracking.

III. KEY IDEA AND GROUNDWORK

A. Medial Axis Transform

We present a brief overview of the MAT theory, highlighting only the aspects relevant to this work. For a more comprehensive treatment, see [18]. As detailed in [19], there are multiple ways to define the MAT, each producing a valid and informative representation. In this work, we employ the most widely recognized definition [20].

Definition 1. Let $\mathcal{O}$ be a connected bounded domain in $\mathbb{R}^2$. The Medial Axis Transform of $\mathcal{O}$ is the set of centers $\mathcal{C}$ and corresponding radii R of all maximally inscribed circles inside $\mathcal{O}$. Each of these circles is tangent to $\mathcal{O}$ at least at two points.

In general, MAT produces a medial representation by characterizing an object's solid geometry as the union of infinitely many circles with varying centers and radii, whose centers form a continuous medial manifold, commonly referred to as the medial axis (see Fig. 2). However, exact MAT computation is generally intractable, and our focus is not on deriving the precise medial representation from a given boundary. Instead, we approximate the medial representation via two spline parameterizations: a continuous medial manifold and a positive scalar thickness field. Together, they facilitate an inside-out analytical reconstruction of the object's boundary.

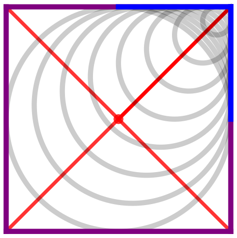

Fig. 2: Example illustration of the MAT of a square. Traditional MAT approaches extract the medial axes (red) from the given object boundary (purple). They intersect at the square's center and mark the loci of infinitely many maximum inscribed circle centers. A representative subset of these circles (gray) is shown, and their envelope reconstructs the square's boundary (blue) analytically in an inside-out fashion.

B. Synthetic Medial Representation

In this subsection, we approximate the medial representation of a two-dimensional object $\mathcal{O} \subset \mathbb{R}^2$ by two bounded Bézier curve parameterizations, namely a smooth medial manifold by a cubic Bézier curve

$$\begin{aligned}\underline{\mathrm{m}}\left(u,\, \underline{\mathrm{P}}_{1:4}\right) = {}& (1-u)^3\, \underline{\mathrm{P}}_1 + 3\,(1-u)^2\, u\, \underline{\mathrm{P}}_2 \\ & + 3\,(1-u)\, u^2\, \underline{\mathrm{P}}_3 + u^3\, \underline{\mathrm{P}}_4 \ ,\end{aligned} \tag{8}$$

where the control points $\{\underline{\mathrm{P}}_i \in \mathbb{R}^2\}_{i=1}^{4}$ control the shape and curvature of the medial axis, and an associated scalar positive thickness field defined by another quadratic Bézier curve

$$\mathrm{R}\left(u,\, \mathrm{r}_{1:3}\right) = (1-u)^2\, \mathrm{r}_1 + 2\,(1-u)\, u\, \mathrm{r}_2 + u^2\, \mathrm{r}_3 \tag{9}$$

with $\{\mathrm{r}_i \in \mathbb{R}\}_{i=1}^{3}$ defining the thickness variation along the medial axis. Both curves share the parameter $u \in [0, 1]$, ensuring a well-defined, bounded parameterization.

C. Inverse Skeletonization

After constructing a synthetic medial representation using two Bézier curves, our method applies the concept of *inverse skeletonization* [21], [22]. In this framework, the medial structure is defined first, and the object boundary is subsequently reconstructed in closed form. We subsequently derive sufficient conditions under which a single manifold, equipped with a positive thickness field, constitutes the complete skeleton of a simple object. When these criteria are satisfied, an explicit parametric expression for the boundary follows analytically.

According to the literature, the inverse skeletonization problem can be formulated as follows.

Definition 2. Given a bounded medial manifold $\mathcal{M}$ equipped with a positive scalar field $\mathcal{R}$, find a simple object $\mathcal{O}$, whose skeleton is given by $\mathcal{M}$ and $\mathcal{R}$, and express the boundary $\partial\mathcal{O}$ of $\mathcal{O}$ as a function of $\mathcal{M}$ and $\mathcal{R}$.

While defining a synthetic medial manifold and its associated thickness field is straightforward, this alone does not ensure a valid skeleton for arbitrary shapes. We therefore analyze the medial geometry to derive the precise conditions under which it constitutes a valid skeleton.

Let the synthetic medial representation, comprising a single medial manifold $\underline{\mathrm{m}}\left(u,\, \underline{\mathrm{P}}_{1:4}\right)$ and a positive scalar thickness field $\mathrm{R}\left(u,\ \mathrm{r}_{1:3}\right)$, accurately model a simple object $\mathcal{O}$. In this setting, each circle centered on the manifold is maximal within $\mathcal{O}$ and is tangent to the true, but unknown, boundary $\partial\mathcal{O}$ at least at two distinct points. Denoting these tangent points by $\underline{\mathrm{Z}} = [\mathrm{Z}_{\mathrm{x}}, \mathrm{Z}_{\mathrm{y}}]^{\top}$, they satisfy the implicit equation

$$\forall \underline{\mathrm{Z}},\ \exists u \in [0,1],\ S(\underline{\mathrm{Z}},\ u) = \|\underline{\mathrm{m}}(u) - \underline{\mathrm{Z}}\|_2^2 - \mathrm{R}^2(u) = 0\ ,$$

ensuring they lie on both the corresponding maximum inscribed circle and the true boundary. As u varies, the loci of these tangency points trace out two continuous envelopes that jointly approximate $\partial\mathcal{O}$. Our reconstruction strategy therefore consists of extracting this envelope of maximum inscribed circles to recover the unknown boundary. In Fig. 2, the blue solid curves exemplify this envelope.

In the following, we restrict our attention to a single envelope of the synthetic medial representation parameterized by $\underline{\mathrm{m}}(u)$ and $\mathrm{R}(u)$, and omit the control points for clarity. To parameterize this envelope, we define a mapping $u \in \mathbb{R} \mapsto \underline{\mathrm{Z}}(u) = [\mathrm{Z}_{\mathrm{x}}(u),\ \mathrm{Z}_{\mathrm{y}}(u)]^{\top} \in \mathbb{R}^2$, which traces the locus $\mathcal{Z} = \{\underline{\mathrm{Z}}(u) \mid u \in [0,1]\}$. By construction, $\underline{\mathrm{Z}}(u)$ must fulfill the following two sufficient conditions [21]

$$S\left(\underline{\mathrm{Z}}(u),\ u\right) = \|\underline{\mathrm{m}}(u) - \underline{\mathrm{Z}}(u)\|_2^2 - \mathrm{R}^2(u) = 0\ , \tag{10}$$

$$\frac{\partial}{\partial u} S\left(\underline{\mathrm{Z}}(u),\ u\right) = 0\ . \tag{11}$$

Recall that the envelope of a circle family is the set of points at which each circle is tangent to its envelope. Hence, every envelope point corresponds uniquely to one maximum inscribed circle, ensuring that condition (10) holds.

To detail the second condition (11), consider the derivative $\left[\frac{d}{du}\mathrm{Z}^{\mathrm{x}}(u),\ \frac{d}{du}\mathrm{Z}^{\mathrm{y}}(u)\right]^{\top}\Big|_{u=u^*}$, which is the tangent vector of the envelope curve $\mathcal{Z}$ at parameter value u^*. The corresponding tangent point on the envelope is $\underline{\mathrm{Z}}(u^*)$. Conversely, the same parameter u^* defines the maximum inscribed circle with center $\underline{\mathrm{m}}\left(u^*\right)$ and radius $\mathrm{R}\left(u^*\right)$. This circle can be written implicitly as $\left\{\underline{\mathrm{P}} \in \mathbb{R}^2 \;\middle|\; S(\underline{\mathrm{P}}, u^*) = 0\right\}$. The outward normal to this circle at any point $\underline{\mathrm{P}}$ is given by the gradient $\left[\frac{\partial}{\partial \mathrm{P}^{\mathrm{x}}} S(\underline{\mathrm{P}}, u^*),\ \frac{\partial}{\partial \mathrm{P}^{\mathrm{y}}} S(\underline{\mathrm{P}}, u^*)\right]^{\top}$. Assuming the synthetic medial representation faithfully models the object's interior, the tangent point $\underline{\mathrm{Z}}(u^*)$ must satisfy $S\left(\underline{\mathrm{Z}}(u^*),\ u^*\right) = 0$. Moreover, the circle's normal at $\underline{\mathrm{Z}}(u^*)$ must be perpendicular to the envelope's tangent at the same parameter value u^*, yielding the orthogonality condition

$$\left[\frac{d}{du}\underline{\mathrm{Z}}(u)\right]^{\top}\Bigg|_{u=u^*} \left[\frac{\partial}{\partial \underline{\mathrm{P}}} S(\underline{\mathrm{P}},\ u^*)\right]\Bigg|_{\underline{\mathrm{P}}=\underline{\mathrm{Z}}(u^*)} = 0\ . \tag{12}$$

From the first condition (10), we have $\frac{d}{du} S\left(\underline{\mathrm{Z}}(u),\ u\right) = 0$. Differentiating $S\left(\underline{\mathrm{Z}}(u),\ u\right)$ with respect to u gives

$$\begin{aligned}\frac{\partial}{\partial \mathrm{Z}^{\mathrm{x}}} S\left(\underline{\mathrm{Z}},\ u\right)\ \frac{d}{du}\mathrm{Z}^{\mathrm{x}}(u) + \frac{\partial}{\partial \mathrm{Z}^{\mathrm{y}}} S\left(\underline{\mathrm{Z}},\ u\right)\ \frac{d}{du}\mathrm{Z}^{\mathrm{y}}(u) \\ + \frac{\partial}{\partial u} S\left(\underline{\mathrm{Z}},\ u\right) = 0\ .\end{aligned}$$

In combination with the zero scalar product condition (12), this confirms that the second sufficient condition (11) is satisfied.

D. Closed-Form Shape Reconstruction

With both sufficient conditions satisfied, our Bézier-based synthetic medial representation yields a robust framework for deriving an exact analytic parametrization of the object boundary. Specifically, for each $u \in [0,1]$, the corresponding maximum inscribed circle is tangent to the object boundary at two points, $\underline{\mathrm{Z}}^{\pm}(u)$, which satisfy the sufficient conditions (10) and (11), and admit the following closed-form expressions

$$\begin{aligned}\underline{\mathrm{Z}}^{\pm}(u) &= \underline{\mathrm{m}}(u) + \mathrm{R}(u)\ \underline{\mathrm{U}}^{\pm}(u)\ , \\ \underline{\mathrm{U}}^{\pm}(u) &= -\nabla_{\mathrm{m}}\mathrm{R}(u) \pm \sqrt{1 - \|\nabla_{\mathrm{m}}\mathrm{R}(u)\|_2^2}\ \underline{\mathrm{N}}_{\mathrm{m}}(u)\ .\end{aligned} \tag{13}$$

A detailed derivation of the above expressions is provided in the Appendix, and an example illustration is shown in Fig. 4. In (13), $\underline{\mathrm{N}}_{\mathrm{m}}(u)$ is the unit normal along the medial manifold. $\nabla_{\mathrm{m}}\mathrm{R}(u)$ projects the gradient of the thickness field onto the tangent direction of the medial manifold. In particular, the gradient of $\mathrm{R}(u)$ with respect to the arc length $\mathrm{s}(u)$ along the medial manifold $\underline{\mathrm{m}}(u)$ is given by

$$\frac{d}{ds}\mathrm{R}(u) = \frac{d\mathrm{R}(u)/du}{ds/du} = \frac{\mathrm{R}'(u)}{\sqrt{[\mathrm{x}'(u)]^2 + [\mathrm{y}'(u)]^2}}\ ,$$

and its projection onto the medial tangent is

$$\begin{aligned}\nabla_{\mathrm{m}}\mathrm{R}(u) &= \frac{d}{ds}\mathrm{R}(u)\ \frac{\underline{\mathrm{m}}'(u)}{\|\underline{\mathrm{m}}'(u)\|_2} \\ &= \frac{\mathrm{R}'(u)}{\sqrt{[\mathrm{x}'(u)]^2 + [\mathrm{y}'(u)]^2}}\ \frac{\underline{\mathrm{m}}'(u)}{\|\underline{\mathrm{m}}'(u)\|_2}\ .\end{aligned}$$

$\underline{\mathrm{U}}^{\pm}(u)$ denotes the unit vector from the circle center to its tangency points $\underline{\mathrm{Z}}^{\pm}(u)$, and the constraint $\|\nabla_{\mathrm{m}}\mathrm{R}(u)\|_2^2 \leq 1$ ensures that the resulting expressions remain real-valued.

Our dual-curve medial formulation combines a parameterized medial manifold with an associated thickness field to produce a smooth and analytically tractable shape reconstruction. More importantly, it contributes significantly to the design of a novel flexible parametric shape model for EOT.

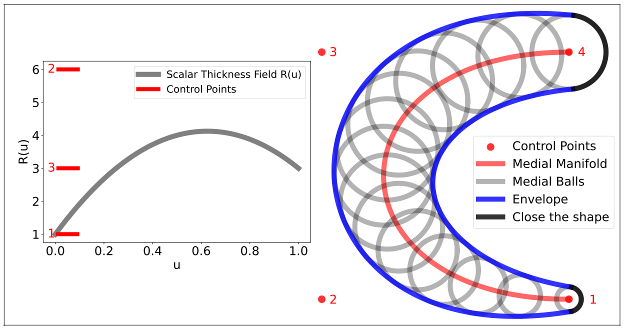

Fig. 3: Example illustration of the reconstructed shape (blue) obtained from the envelope of all maximum inscribed circles. These circles are produced by a smooth, continuous medial manifold (red) and a positive thickness field (gray), ensuring a smooth and analytically consistent shape representation.

IV. METHOD DERIVATION

So far, we have established the theoretical foundation of this work. In this section, we develop our Stochastic Medial Axis Transform framework for extended object tracking.

A. State Parameterization

Given that the shape model, comprising two Bézier curves, is stochastically associated with noisy measurements, the uncertainty in their control points is captured by the random vector $\underline{\boldsymbol{x}}^{\text{ext.}}$ within (1). The model's representational flexibility depends directly on the number and placement of control points. Increasing them improves expressiveness and adaptability, but leads to higher computational cost in state estimation. To balance expressiveness and efficiency, we employ a cubic Bézier curve with four control points $\underline{\mathbf{P}}_{1:4}$ for the medial manifold and a quadratic Bézier curve with three control points $\mathbf{r}_{1:3}$ for the thickness field, as expressed in

$$\underline{\boldsymbol{x}}_k^{\text{ext.}} = [\mathbf{P}_1^x,\ \mathbf{P}_1^y,\ \ldots,\ \mathbf{P}_4^x,\ \mathbf{P}_4^y,\ \mathbf{r}_1,\ \mathbf{r}_2,\ \mathbf{r}_3]\ . \tag{14}$$

For elongated, curved extended targets, accurately capturing variations in length and curvature is considerably more important than accounting for minor width variations. Consequently, our approach prioritizes enhanced flexibility in modeling changes along the object's length and curvature.

B. Explicit Likelihood Function

Based on the analytical boundary definition in (13), obtained via our synthetic medial representation and inverse skeletonization, the generative measurement model (2) becomes

$$\underline{\boldsymbol{y}}_k = \underline{\mathbf{Z}}^{\pm}(u,\ \underline{\boldsymbol{x}}_k) + \underline{\boldsymbol{v}}_k\ . \tag{15}$$

Assuming additive Gaussian noise with covariance matrix $\Sigma^{\boldsymbol{v}}$, the explicit likelihood for a concrete measurement $\underline{\tilde{y}}_k$, namely $f_k^{\mathrm{L}}(\underline{x}_k) = f_k^{\boldsymbol{y}}(\underline{\tilde{y}}_k \mid \underline{x}_k)$, can be easily computed. The derivation proceeds as follows

$$\begin{aligned}
f_k^{\boldsymbol{y}}(\underline{y}_k \mid \underline{x}_k) &= \int_{\mathbb{R}^2} f(\underline{y}_k,\ \underline{v}_k \mid \underline{x}_k)\ \mathrm{d}\underline{v}_k \\
&= \int_{\mathbb{R}^2} \delta\left(\underline{y}_k - \underline{\mathrm{Z}}^{\pm}(u,\ \underline{x}_k) - \underline{v}_k\right)\ f_k^{\boldsymbol{v}}(\underline{v}_k)\ \mathrm{d}\underline{v}_k \\
&= f_k^{\boldsymbol{v}}\left(\underline{y}_k - \underline{\mathrm{Z}}^{\pm}(u,\ \underline{x}_k)\right) \\
&= \mathcal{N}_{\boldsymbol{v}}\left(\underline{y}_k\, ;\, \underline{\mathrm{Z}}^{\pm}(u,\ \underline{x}_k)\, ,\, \Sigma^{\boldsymbol{v}}\right)\ ;
\end{aligned} \tag{16}$$

$$\begin{aligned}
f_k^{\mathrm{L}}(\underline{x}_k) &= f_k^{\boldsymbol{y}}(\underline{\tilde{y}}_k \mid \underline{x}_k) = \mathcal{N}_{\boldsymbol{v}}\left(\underline{\tilde{y}}_k\, ;\, \underline{\mathrm{Z}}^{\pm}(u,\ \underline{x}_k)\, ,\, \Sigma^{\boldsymbol{v}}\right)\ , \\
f(\mathcal{Y}_k \mid \underline{x}_k) &= f\left(\{\underline{\tilde{y}}_{k,i}\}_{i=1}^{N_k} \,\middle|\, \underline{x}_k\right) = \prod_{i=1}^{N_k} f_{k,i}^{\boldsymbol{y}}\left(\underline{\tilde{y}}_{k,i} \mid \underline{x}_k\right) \\
&= \prod_{i=1}^{N_k} \mathcal{N}_{\boldsymbol{v}}\left(\underline{\tilde{y}}_{k,i}\, ;\, \underline{\mathrm{Z}}^{\pm}(u,\ \underline{x}_k)\, ,\, \Sigma^{\boldsymbol{v}}\right)\ .
\end{aligned} \tag{17}$$

C. Measurement Association Solution

Nonetheless, several challenges remain. Due to the sensor noise, directly associating individual measurements with the system state is problematic. Specifically, each position measurement must be matched to its corresponding maximum inscribed circle, i.e., the parameter $u \in [0, 1]$, and to the correct tangency point on it, $\underline{\mathbf{Z}}^{+}$ or $\underline{\mathbf{Z}}^{-}$. Consequently, further assumptions regarding the measurement source must be introduced. Once this association issue is resolved, the likelihood in (17) can be directly incorporated into the recursive Bayesian estimator detailed in Subsection IV-E.

In this work, we adopt the widely used Greedy Association Model (GAM) framework [23], [24] to address the measurement source association problem. It requires no prior assumptions on how measurement sources are distributed along the target boundary. Instead of considering solely distance-based criteria, we integrate the analytic medial structure and minimize a collinearity-based cost that incorporates both distance and angular consistency with the local boundary.

In our implementation, each measurement $\underline{\tilde{y}}_k$ is first associated with its corresponding envelope curve. Hence, we conduct a grid search over discretized values of $u \in [0, 1]$ and compute the inscribed-circle center $\underline{\mathbf{m}}_k(u,\ \underline{\boldsymbol{x}}_k)$ and its two tangency points $\underline{\mathbf{Z}}_k^{\pm}(u,\ \underline{\boldsymbol{x}}_k)$. We then define the vectors $\underline{\boldsymbol{a}}_k \overset{\text{def}}{=} \underline{\tilde{y}}_k - \underline{\mathbf{m}}_k(u,\ \underline{\boldsymbol{x}}_k)$, $\underline{\boldsymbol{b}}_k^{\pm} \overset{\text{def}}{=} \underline{\mathbf{Z}}_k^{\pm}(u,\ \underline{\boldsymbol{x}}_k) - \underline{\mathbf{m}}_k(u,\ \underline{\boldsymbol{x}}_k)$, and evaluate the angles between $\underline{\boldsymbol{a}}_k$ and $\underline{\boldsymbol{b}}_k^{\pm}$, given by

$$\theta_k^{\pm}(u) = \arccos\left(\frac{\underline{\boldsymbol{a}}_k^{\top}\ \underline{\boldsymbol{b}}_k^{\pm}}{\|\underline{\boldsymbol{a}}_k\|_2\ \|\underline{\boldsymbol{b}}_k^{\pm}\|_2}\right)\ . \tag{18}$$

For each $u \in [0, 1]$, the candidate tangency point is chosen as

$$\underline{\mathbf{Z}}_k(u,\ \underline{\boldsymbol{x}}_k) = \begin{cases} \underline{\mathbf{Z}}_k^{-}(u,\ \underline{\boldsymbol{x}}_k), & \text{if } \theta_k^{+}(u) \leq \theta_k^{-}(u), \\ \underline{\mathbf{Z}}_k^{+}(u,\ \underline{\boldsymbol{x}}_k), & \text{otherwise.} \end{cases} \tag{19}$$

Next, we exploit the geometric properties of the synthetic medial representation to determine the correct parameter value u^* corresponding to $\underline{\tilde{y}}_k$. According to (13), $\underline{\boldsymbol{b}}_k$ is expressed as $\mathbf{R}_k(u)\,\underline{\mathbf{U}}_k(u)$, which is aligned with the local normal at $\underline{\mathbf{m}}_k(u)$. Under the specific assumption that $\underline{\tilde{y}}_k$ lies on the normal ray through $\underline{\mathbf{m}}_k(u)$ and $\underline{\mathbf{Z}}_k(u)$, the points $\underline{\tilde{y}}_k$, $\underline{\mathbf{m}}_k(u)$ and $\underline{\mathbf{Z}}_k(u)$ must be collinear. The following cross product magnitude is computed for each u as the evaluation metric

$$C_k(u) = \left|[\underline{\tilde{y}}_k - \underline{\mathbf{m}}_k(u)] \times [\underline{\mathbf{Z}}_k(u) - \underline{\mathbf{m}}_k(u)]\right|\ . \tag{20}$$

The optimal parameter u^* is obtained by minimizing the collinearity metric $C_k(u)$ over the search interval. An illustrative example is provided in Fig. 4.

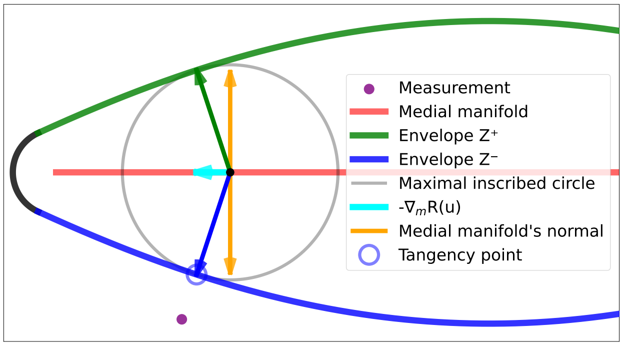

Fig. 4: Example illustration of measurement-source association. Given a position measurement (purple), the envelope curve (blue) that could contain its source is identified first. After evaluating a geometric collinearity metric (20) over the parameter u, the optimal maximum inscribed circle (gray) and its corresponding tangency point (blue circle) on this envelope are determined. This procedure resolves source association in a simple, principled manner, without any prior assumptions on source distribution.

D. Constraints on Extent Parameters

In EOT, shape and extent parameters are often constrained to predefined intervals, posing challenges in practical estimation. Within the SMAT framework, enforcing strictly positive radii for all maximum inscribed circles is essential. We model the thickness field as a quadratic Bézier curve over $u \in [0, 1]$, where the control points $\{\mathbf{r}_i \in \mathbb{R}\}_{i=1}^3$ define a convex combination. Therefore, the thickness values remain strictly positive if and only if all three scalars $\{\mathbf{r}_i \in \mathbb{R}\}_{i=1}^3$, which themselves are part of the state vector, are strictly positive. However, enforcing such positivity constraints in common nonlinear Kalman filters is challenging due to their unbounded support. Inspired by [25], we address this by applying a bijective, monotonically increasing state transformation function to each $\mathbf{r}_i$, allowing the filter to operate on unconstrained variables while guaranteeing $\mathbf{r}_i > 0$:

$$\mathrm{t}(x) = \begin{cases} x + \log\left(1 + e^{-x}\right), & x > 0 \; ; \\ \log\left(1 + e^{x}\right), & x \leq 0 \; . \end{cases} \tag{21}$$

This function is widely used as a neural network's activation function [26]. A continuous piecewise-defined alternative appears in [25], but its first derivative is non-smooth at the origin and its second derivative is discontinuous. In contrast, our formulation is infinitely differentiable and ensures that the function and all its derivatives vary smoothly across $\mathbb{R}$.

Moreover, the first derivative of our transformation function

$$\mathrm{t}'(x) = \frac{e^x}{1 + e^x} \; , \tag{22}$$

is strictly bounded within $(0, 1)$ for all $x \in \mathbb{R}$. Hence, infinitesimal input perturbations are not exponentially amplified, as they would be under the mapping $x \mapsto e^x$, but are instead attenuated by its bounded slope. This leads to corresponding likelihood values that vary within a moderate range, which is an essential property for Bayesian filters that employ likelihoods explicitly for inference, such as the PGF [13]. It relies on log-likelihood magnitudes to determine progression step sizes during measurement updates. Importantly, our transformation (21) preserves the sample spread without significantly distorting the likelihood landscape.

Besides, as inputs grow, the function (21) closely approximates the identity function $\mathrm{t}(x) = x$ as the additive term $\log\left(1 + e^{-x}\right)$ rapidly vanishes.

Additionally, we impose another geometric constraint for a valid shape reconstruction, namely $\|\nabla_{\mathrm{m}} \mathbf{R}(u)\|_2^2 \leq 1$ in (13). This constraint is relatively complex and cannot be directly implemented through a simple parameter transformation. Upon closer examination, it can be expressed as

$$\frac{[\mathbf{R}'(u)]^2}{[\mathbf{x}'(u)]^2 + [\mathbf{y}'(u)]^2} \leq 1 \;\rightarrow\; |\mathbf{R}'(u)| \leq \|\underline{\mathbf{m}}'(u)\|_2 \; . \tag{23}$$

The thickness field should not vary faster than the medial manifold w.r.t. the parameter u. For elongated targets, our modeling has already prioritized accurately capturing variations in length and curvature by assigning more control points to the medial manifold. In contrast, the thickness field inherently exhibits smoother and slower variations. As a result, the inequality (23) is satisfied by construction.

E. Recursive Bayesian State Estimation

By introducing appropriate assumptions within the GAM framework, we effectively resolve the measurement-source association problem. Besides, to enforce parameter constraints, a smooth state transformation is introduced to allow estimation in an unbounded state space, thus yielding constrained parameter estimates. Based on these results, the explicit likelihood in (17) is employed, and the PGF [13] is selected for recursive Bayesian inference, benefiting from its superior accuracy and computational efficiency.

V. EVALUATION

In this section, we assess the proposed SMAT's ability to track arbitrary target shapes, whether convex or non-convex, symmetric or asymmetric, using synthetic data corrupted by isotropic Gaussian noise. We restrict our evaluation to closed shapes of finite size that contain no holes. Performance is quantified via the intersection over union (IoU) between the estimated boundary $\partial\mathcal{O}_k$ and the ground-truth boundary $\partial\mathcal{O}_k^{\mathrm{GT}}$

$$\mathrm{IoU}_k = \frac{\mathrm{Area}(\partial\mathcal{O}_k \,\cap\, \partial\mathcal{O}_k^{\mathrm{GT}})}{\mathrm{Area}(\partial\mathcal{O}_k \,\cup\, \partial\mathcal{O}_k^{\mathrm{GT}})} \; . \tag{24}$$

For numerical evaluations, each continuous closed curve is approximated by a polygonal boundary composed of line segments, which allows direct computation of intersection and union areas. An IoU of 1 indicates perfect overlap, while 0 implies no overlap at all. In our experiments, IoU serves as a high-level qualitative performance indicator rather than an exact quantitative metric.

For simplicity, we evaluated two static targets: a convex symmetric shape and a non-convex asymmetric shape. Extending to dynamic scenarios requires propagating the augmented state estimates through a stochastic motion model. For comparison, we applied a non-parametric extent model via recursive Gaussian Process (GP) regression [8] to the same measurement sets. During each measurement update, the analytic posterior GP model conditioned on all concrete measurements estimates the target boundary in closed-form. This flexible GP-based approach serves as a benchmark against our method.

Fig. 5 and Fig. 6 depict two representative runs. In each figure, subplots (a-d) illustrate the results produced by our method. In both cases, we initialize our filter with a deliberately conservative, enclosing shape. Specifically, we model the medial manifold as a straight segment and assign a uniform radius that fully contains the first batch of measurements. Such an initialization deployed in the absence of a precise prior allows the estimator to freely shrink and bend the shape inward toward the ground truth. Empirically, this accelerates IoU convergence and enhances robustness, especially when tracking challenging non-convex shapes. Fig. 7 plots the IoU values over 50 time steps, demonstrating that our method rapidly reaches high overlap across both target geometries. Nevertheless, in the non-convex asymmetric case, the GP-based method fails to achieve comparable results.

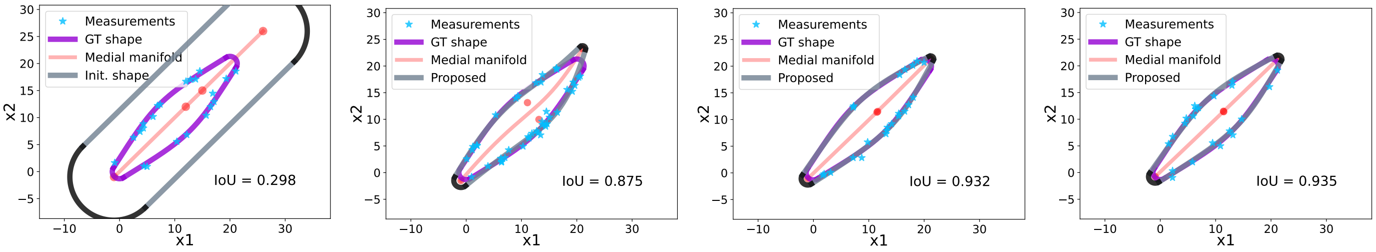

(a) SMAT: Initialization (b) SMAT: 15th time step (c) SMAT: 35th time step (d) SMAT: 50th time step

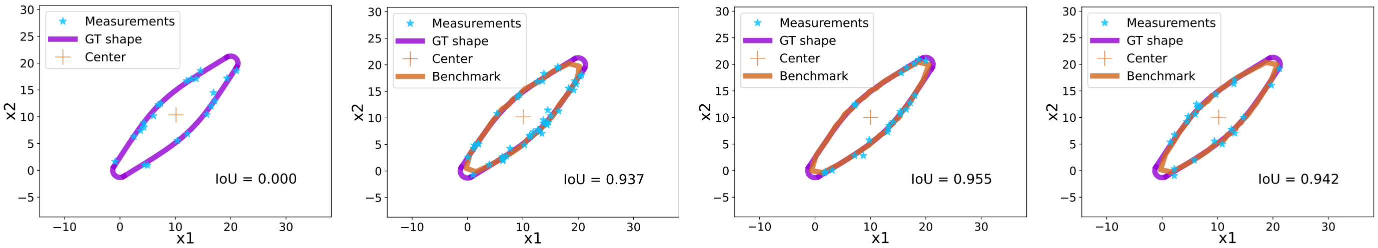

(e) GP-EOT: Initialization (f) GP-EOT: 15th time step (g) GP-EOT: 35th time step (h) GP-EOT: 50th time step

Fig. 5: Recursive tracking of a static, elongated, convex, and symmetric target from noisy boundary measurements (blue). Subplots (a-d) show four milestones obtained with the proposed SMAT framework, namely initialization and the 15th, 35th, and 50th time steps. SMAT starts from a deliberately enclosing envelope (gray), whose medial manifold is a straight line segment (red). As new measurements arrive, the estimate (gray) rapidly contracts and bends toward the ground-truth boundary (purple). Subplots (e-h) present the GP-based benchmark (brown) applied to the identical sets of boundary measurements. Its online recursive GP regression, combined with the absence of an explicit time-consuming measurement–source association procedure, allows for faster convergence.

A. *Computational Complexity Analysis*

To complement the qualitative results, we analyzed the algorithmic cost of each stage executed within the recursive estimation loop. Let d be the state dimension, M_k the number of measurements at time step k, N_u the grid resolution over the interval $[0, 1]$ for the measurement association, N_s the number of deterministic Gaussian samples per progression in the PGF, and $\mathrm{P}_{\max}$ the maximum number of PGF recursions.

1) Prediction Step: Under the static target assumption, the time update reduces to preserving the previous posterior state PDF while augmenting it with process noise. These operations require $\mathcal{O}(\mathrm{d}^2)$ time and memory complexity, respectively.

2) Measurement Association: Each measurement undergoes an exhaustive search over N_u uniform grid points, with each geometric evaluation costing $\mathcal{O}(1)$. This yields a total time complexity of $\mathcal{O}(\mathrm{M}_k \cdot \mathrm{N}_u)$ per measurement update. The algorithm stores one candidate tuple per grid point, each consisting of a scalar parameter u and geometric vectors. This results in the same $\mathcal{O}(\mathrm{M}_k \cdot \mathrm{N}_u)$ space complexity.

3) Filtering: The dominant cost within a single progression step of the PGF arises from evaluating likelihoods over all N_s samples and M_k measurements, resulting in a time complexity of $\mathcal{O}(\mathrm{N}_s \cdot \mathrm{M}_k)$ and a space complexity of $\mathcal{O}(\mathrm{d} \cdot \mathrm{N}_s)$ for storing the samples. Thus, the overall complexity per time step is $\mathcal{O}(\mathrm{P}_{\max} \cdot \mathrm{N}_s \cdot \mathrm{M}_k)$ in time and $\mathcal{O}(\mathrm{d} \cdot \mathrm{N}_s)$ in space.

TABLE I: Computational complexities of individual modules within the proposed SMAT framework.

Module	**Time Complex.**	**Space Complex.**
Time Update	$\mathcal{O}(\mathrm{d}^2)$	$\mathcal{O}(\mathrm{d}^2)$
Measurement Association	$\mathcal{O}(\mathrm{M}_k \cdot \mathrm{N}_u)$	$\mathcal{O}(\mathrm{M}_k \cdot \mathrm{N}_u)$
Filtering with PGF [13]	$\mathcal{O}(\mathrm{P}_{\max} \cdot \mathrm{N}_s \cdot \mathrm{M}_k)$	$\mathcal{O}(\mathrm{d} \cdot \mathrm{N}_s)$

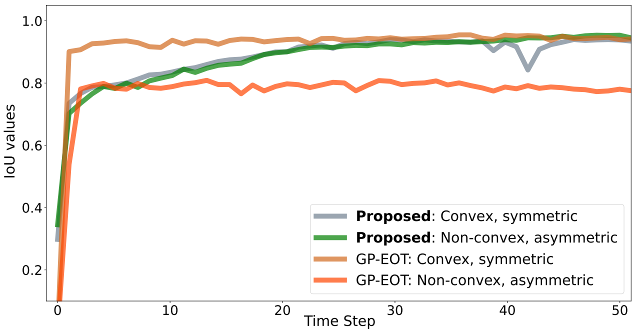

Fig. 7: Illustration of the IoU evolution for two distinct target geometries. In both cases, the proposed SMAT approach consistently converges to higher IoU levels. While the GP-based benchmark exhibits faster convergence in the convex scenario, its performance degrades markedly in the non-convex case.

VI. CONCLUSION

In this paper, we introduce SMAT, a novel extension of traditional MAT theory that reformulates the generally infeasible computation of the exact medial representation as a tractable stochastic Bayesian state estimation problem. All model parameters are estimated recursively over time. Based on this formulation, a target boundary can be reconstructed analytically by first internally parameterizing a synthetic medial representation via two continuous Bézier curves: one for the medial manifold, defining the centers of maximum inscribed circles, and the other for the thickness field, assigning positive radii to these centers. Subsequently, an inverse skeletonization process is applied to recover the external boundary as the envelope formed by the union of all such inscribed circles. Our flexible parametric shape model supports a wide range of geometries, including convex, non-convex, symmetric, and asymmetric forms.

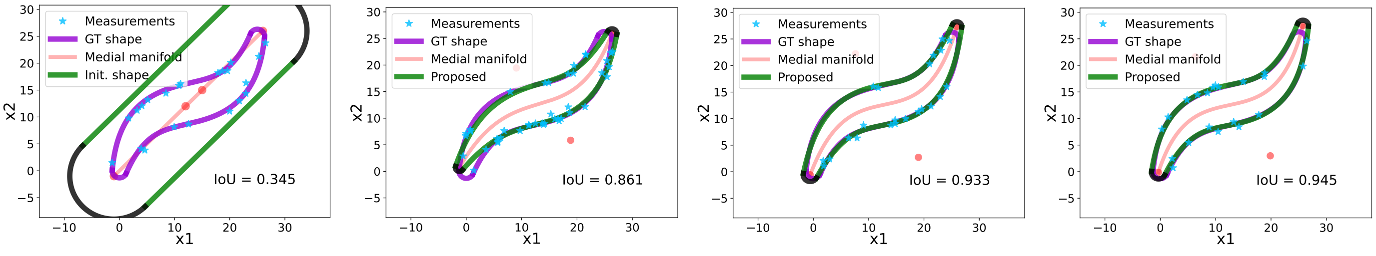

(a) SMAT: Initialization (b) SMAT: 15th time step (c) SMAT: 35th time step (d) SMAT: 50th time step

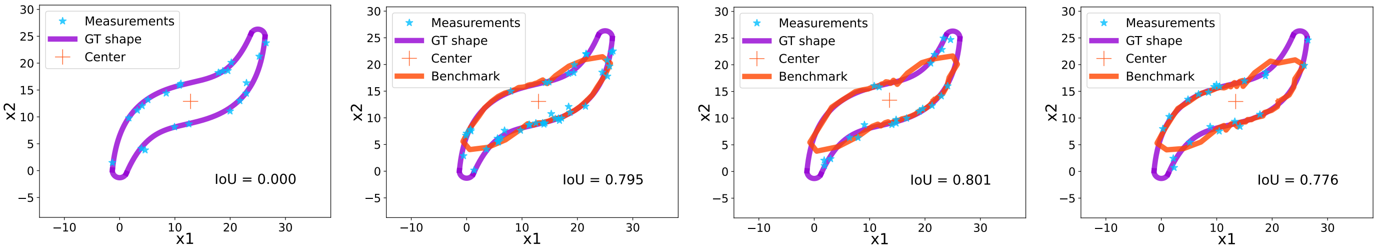

(e) GP-EOT: Initialization (f) GP-EOT: 15th time step (g) GP-EOT: 35th time step (h) GP-EOT: 50th time step

Fig. 6: Recursive tracking of a static, elongated, non-convex, and asymmetric target from noisy boundary measurements (blue). A similar initialization strategy for the SMAT is adopted, composed of a deliberately enclosing envelope (green) with a straight line segment (red) as the medial manifold. Our method converges gradually toward the challenging non-convex ground-truth shape (purple), showing its robustness in handling complex geometries. In contrast, the GP-based approach (orange) struggles with non-convex geometries and fails to achieve comparable results, despite its flexible non-parametric shape model.

Several limitations of our current approach remain to be addressed in future work. The analytic reconstruction in (13) yields two curve branches, $\underline{\mathrm{Z}}^{+}(u)$ and $\underline{\mathrm{Z}}^{-}(u)$, both parameterized over $u \in [0,1]$. However, at the endpoints $u = 0$ and $u = 1$, the maximum inscribed circle contacts the outer envelope along entire continuous arcs, producing infinitely many tangency points rather than a single one. These arcs, depicted as black solid curves in Fig. 3, are not explicitly parameterized in the current shape model. Consequently, measurements originating from this ambiguous region may be misattributed to the $\underline{\mathrm{Z}}^{+}(u)$ and $\underline{\mathrm{Z}}^{-}(u)$ branches.

The employed GAM method suffers from the *length problem* introduced in [15], where the reconstructed shape could diverge and expand infinitely outward along the envelope's normal direction without correction. A potential remedy is to use Spatial Distribution Models, which implicitly associate measurements with all potential sources. Additionally, *negative* measurements [27], which are known not to originate from the object, are useful and can further constrain the estimation by excluding regions where the object cannot be located.

Generalizing the SMAT to three-dimensional space and extending it to support multiple medial manifolds stemming from a single junction enables capturing a broader spectrum of geometries. This extension offers multiple advantages, including more accurate shape analysis of particulate solids.

VII. ACKNOWLEDGMENTS

The IGF project 01IF22901N of the research association Forschungs-Gesellschaft Verfahrenstechnik e. V. (GVT) is supported in a program to promote Industrial Collective Research (IGF) by the Federal Ministry of Economic Affairs and Climate Action on the basis of a decision of the German Bundestag.

APPENDIX

To establish that the closed-form solutions in (13) rigorously satisfy both sufficient conditions (10) and (11) for inverse skeletonization, and thus provide stronger support for our derivation, we proceed as follows. First, we verify the first sufficient condition (10).

$$\begin{aligned}\langle \nabla_{\mathrm{m}}\mathrm{R}(u),\ \underline{\mathrm{N}}_{\mathrm{m}}(u)\rangle &= \nabla_{\mathrm{m}}^{\top}\mathrm{R}(u)\ \underline{\mathrm{N}}_{\mathrm{m}}(u)\\ &= \frac{d}{ds}\mathrm{R}(u)\ \underbrace{\underline{\mathrm{T}}_{\mathrm{m}}^{\top}(u)\ \underline{\mathrm{N}}_{\mathrm{m}}(u)}_{=0} = 0\ ,\end{aligned}$$

$$\begin{aligned}S\left(\underline{\mathrm{Z}}^{\pm}(u), u\right) &= \left\|\underline{\mathrm{m}}(u) - \underline{\mathrm{Z}}^{\pm}(u)\right\|_2^2 - \mathrm{R}^2(u)\\ &= \left\|\mathrm{R}(u)\ \underline{\mathrm{U}}^{\pm}(u)\right\|_2^2 - \mathrm{R}^2(u)\\ &= \mathrm{R}^2(u)\left\|-\nabla_{\mathrm{m}}\mathrm{R}(u) \pm \sqrt{1-\|\nabla_{\mathrm{m}}\mathrm{R}(u)\|_2^2}\ \underline{\mathrm{N}}_{\mathrm{m}}(u)\right\|_2^2\\ &\quad - \mathrm{R}^2(u)\\ &= \mathrm{R}^2(u)\ \|\nabla_{\mathrm{m}}\mathrm{R}(u)\|_2^2 - \mathrm{R}^2(u)\\ &\quad + \mathrm{R}^2(u)\ \underbrace{\left\|\sqrt{1-\|\nabla_{\mathrm{m}}\mathrm{R}(u)\|_2^2}\ \underline{\mathrm{N}}_{\mathrm{m}}(u)\right\|_2^2}_{=1-\|\nabla_{\mathrm{m}}\mathrm{R}(u)\|_2^2}\\ &\quad \mp 2\,\mathrm{R}^2(u)\ \sqrt{1-\|\nabla_{\mathrm{m}}\mathrm{R}(u)\|_2^2}\ \underbrace{\langle \nabla_{\mathrm{m}}\mathrm{R}(u), \underline{\mathrm{N}}_{\mathrm{m}}(u)\rangle}_{=0}\\ &= 0 \rightarrow \text{The first sufficient condition is satisfied.}\end{aligned}$$

Having verified the first condition, we now address the second sufficient condition (11), which can be equivalently formulated as

$$\begin{aligned}\frac{\partial}{\partial u}S\left(\underline{\mathrm{Z}}(u),\ u\right) &= \frac{\partial}{\partial u}\left\|\underline{\mathrm{m}}(u) - \underline{\mathrm{Z}}(u)\right\|_2^2 - \frac{\partial}{\partial u}\mathrm{R}^2(u)\\ &= 2\left[\underline{\mathrm{m}}(u) - \underline{\mathrm{Z}}(u)\right]^{\top}\frac{d\,\underline{\mathrm{m}}(u)}{du} - 2\,\mathrm{R}(u)\,\frac{d\,\mathrm{R}(u)}{du}\\ &= 0\ . \end{aligned} \tag{25}$$

Next, we introduce the closed-form expressions from (13)

$$
\begin{aligned}
\frac{\underline{\mathrm{Z}}^{\pm} - \underline{\mathrm{m}}(u)}{\mathrm{R}(u)} &= \underline{\mathrm{U}}^{\pm}(u) \\
&= -\nabla_{\mathrm{m}}\mathrm{R}(u) \pm \sqrt{1 - \|\nabla_{\mathrm{m}}\mathrm{R}(u)\|_2^2}\; \underline{\mathrm{N}}_{\mathrm{m}}(u) \\
&= -\frac{d}{d\mathrm{s}}\mathrm{R}(u)\; \underline{\mathrm{T}}_{\mathrm{m}}(u) \pm \sqrt{1 - \|\nabla_{\mathrm{m}}\mathrm{R}(u)\|_2^2}\; \underline{\mathrm{N}}_{\mathrm{m}}(u)
\end{aligned}
$$

into (25). Leveraging the orthonormality and unit-norm properties of the medial tangent and normal vectors, we reach the following result

$$
\begin{aligned}
\left[\frac{\underline{\mathrm{Z}}^{\pm}(u) - \underline{\mathrm{m}}(u)}{\mathrm{R}(u)}\right]^{\top} \frac{d\underline{\mathrm{m}}(u)}{du} &= -\frac{d}{d\mathrm{s}}\mathrm{R}(u)\; \underline{\mathrm{T}}_{\mathrm{m}}^{\top}(u)\; \frac{d\underline{\mathrm{m}}(u)}{du} \\
&\qquad \pm \sqrt{1 - \|\nabla_{\mathrm{m}}\mathrm{R}(u)\|_2^2}\; \underline{\mathrm{N}}_{\mathrm{m}}^{\top}(u)\; \frac{d\underline{\mathrm{m}}(u)}{du} \\
&= -\frac{d}{d\mathrm{s}}\mathrm{R}(u)\; \underbrace{\underline{\mathrm{T}}_{\mathrm{m}}^{\top}(u)\, \underline{\mathrm{T}}_{\mathrm{m}}(u)}_{=1}\; \left\|\underline{\mathrm{m}}'(u)\right\|_2 \\
&\qquad \pm \sqrt{1 - \|\nabla_{\mathrm{m}}\mathrm{R}(u)\|_2^2}\; \underbrace{\underline{\mathrm{N}}_{\mathrm{m}}^{\top}(u)\, \underline{\mathrm{T}}_{\mathrm{m}}(u)}_{=0}\; \left\|\underline{\mathrm{m}}'(u)\right\|_2 \\
&= -\frac{d\mathrm{R}(u)/du}{ds/du}\; \sqrt{[\mathrm{x}'(u)]^2 + [\mathrm{y}'(u)]^2} \\
&= -\frac{\mathrm{R}'(u)}{\sqrt{[\mathrm{x}'(u)]^2 + [\mathrm{y}'(u)]^2}}\; \sqrt{[\mathrm{x}'(u)]^2 + [\mathrm{y}'(u)]^2} \\
&= -\mathrm{R}'(u) = -\frac{d\mathrm{R}(u)}{du}\; .
\end{aligned}
$$

After straightforward algebraic manipulations, the second sufficient condition (11) is fulfilled

$$
\begin{aligned}
\frac{\partial}{\partial u} S\left(\underline{\mathrm{Z}}(u),\; u\right) &= 2\; \left[\underline{\mathrm{m}}(u) - \underline{\mathrm{Z}}(u)\right]^{\top} \frac{d\,\underline{\mathrm{m}}(u)}{du} - 2\,\mathrm{R}(u)\, \frac{d\,\mathrm{R}(u)}{du} \\
&= 0\; .
\end{aligned}
$$

REFERENCES

[1] Florian Faion, Antonio Zea, Marcus Baum, and Uwe D. Hanebeck. “Bayesian Estimation of Line Segments”. In: *Proceedings of the IEEE ISIF Workshop on Sensor Data Fusion: Trends, Solutions, Applications (SDF 2014)*. Bonn, Germany, Oct. 2014. DOI: 10.1109/SDF.2014.6954710.

[2] Hauke Kaulbersch, Jens Honer, and Marcus Baum. “A Cartesian B-spline vehicle model for extended object tracking”. In: *2018 21st International Conference on Information Fusion (Fusion 2018)*. IEEE. 2018, pp. 1–5.

[3] Michael Feldmann and Dietrich Franken. “Tracking of extended objects and group targets using random matrices—a new approach”. In: *2008 11th International Conference on Information Fusion (Fusion 2008)*. IEEE. 2008, pp. 1–8.

[4] Michael Feldmann and Dietrich Franken. “Advances on tracking of extended objects and group targets using random matrices”. In: *2009 12th International Conference on Information Fusion (Fusion 2009)*. IEEE. 2009, pp. 1029–1036.

[5] Marcus Baum and Uwe D. Hanebeck. “Random Hypersurface Models for Extended Object Tracking”. In: *Proceedings of the 9th IEEE International Symposium on Signal Processing and Information Technology (ISSPIT 2009)*. Ajman, United Arab Emirates, Dec. 2009. DOI: 10.1109/ISSPIT.2009.5407526.

[6] Marcus Baum, Benjamin Noack, and Uwe D. Hanebeck. “Extended Object and Group Tracking with Elliptic Random Hypersurface Models”. In: *Proceedings of the 13th International Conference on Information Fusion (Fusion 2010)*. Edinburgh, United Kingdom, July 2010. DOI: 10.1109/icif.2010.5711854.

[7] Marcus Baum and Uwe D. Hanebeck. “Shape Tracking of Extended Objects and Group Targets with Star-Convex RHMs”. In: *Proceedings of the 14th International Conference on Information Fusion (Fusion 2011)*. Chicago, Illinois, USA, July 2011.

[8] Niklas Wahlström and Emre Özkan. “Extended target tracking using Gaussian processes”. In: *IEEE Transactions on Signal Processing* 63.16 (2015), pp. 4165–4178.

[9] Simon J. Julier and Jeffrey K. Uhlmann. “Unscented Filtering and Nonlinear Estimation”. In: *Proceedings of the IEEE* 92.3 (2004), pp. 401–422. DOI: 10.1109/JPROC.2003.823141.

[10] Jannik Steinbring and Uwe D. Hanebeck. “LRKF Revisited: The Smart Sampling Kalman Filter (S2KF)”. In: *Journal of Advances in Information Fusion* 9.2 (Dec. 2014), pp. 106–123.

[11] Jannik Steinbring and Uwe D. Hanebeck. “S2KF: The Smart Sampling Kalman Filter”. In: *Proceedings of the 16th International Conference on Information Fusion (Fusion 2013)*. Istanbul, Turkey, July 2013.

[12] Uwe D. Hanebeck. “PGF 42: Progressive Gaussian Filtering with a Twist”. In: *Proceedings of the 16th International Conference on Information Fusion (Fusion 2013)*. Istanbul, Turkey, 2013, pp. 1103–1110.

[13] Jannik Steinbring and Uwe D. Hanebeck. “Progressive Gaussian Filtering Using Explicit Likelihoods”. In: *Proceedings of the 17th International Conference on Information Fusion (Fusion 2014)*. Salamanca, Spain, July 2014.

[14] Jannik Steinbring, Marcus Baum, Antonio Zea, Florian Faion, and Uwe D. Hanebeck. “A Closed-Form Likelihood for Particle Filters to Track Extended Objects with Star-Convex RHMs”. In: *Proceedings of the 2015 IEEE International Conference on Multisensor Fusion and Integration for Intelligent Systems (MFI 2015)*. San Diego, California, USA, Sept. 2015. DOI: 10.1109/MFI.2015.7295740.

[15] Antonio Zea, Florian Faion, and Uwe D. Hanebeck. “Tracking Elongated Extended Objects Using Splines”. In: *Proceedings of the 19th International Conference on Information Fusion (Fusion 2016)*. Heidelberg, Germany, July 2016.

[16] Nina Amenta and Marshall Bern. “Surface reconstruction by Voronoi filtering”. In: *Proceedings of the fourteenth annual symposium on Computational geometry*. 1998, pp. 39–48.

[17] Pan Li, Bin Wang, Feng Sun, Xiaohu Guo, Caiming Zhang, and Wenping Wang. “Q-mat: Computing medial axis transform by quadratic error minimization”. In: *ACM Transactions on Graphics (TOG)* 35.1 (2015), pp. 1–16.

[18] Hyeong In Choi, Sung Woo Choi, and Hwan Pyo Moon. “Mathematical theory of medial axis transform”. In: *pacific journal of mathematics* 181.1 (1997), pp. 57–88.

[19] Andrea Tagliasacchi, Thomas Delame, Michela Spagnuolo, Nina Amenta, and Alexandru Telea. “3d skeletons: A state-of-the-art report”. In: *Computer Graphics Forum*. Vol. 35. 2. Wiley Online Library. 2016, pp. 573–597.

[20] Mehrdad Ghatrehnaby and Behrooz Arezoo. “Automatic piloting in progressive dies using medial axis transform”. In: *Applied Mathematical Modelling* 34.10 (2010), pp. 2981–2997.

[21] Paul A Yushkevich, Hui Zhang, and James C Gee. “Continuous medial representation for anatomical structures”. In: *IEEE transactions on medical imaging* 25.12 (2006), pp. 1547–1564.

[22] James Damon. “Smoothness and geometry of boundaries associated to skeletal structures I: Sufficient conditions for smoothness”. In: *Annales de l’institut Fourier*. Vol. 53. 6. 2003, pp. 1941–1985.

[23] Florian Faion, Antonio Zea, and Uwe D. Hanebeck. “Reducing Bias in Bayesian Shape Estimation”. In: *Proceedings of the 17th International Conference on Information Fusion (Fusion 2014)*. Salamanca, Spain, July 2014.

[24] Florian Faion, Antonio Zea, Marcus Baum, and Uwe D. Hanebeck. “Partial Likelihood for Unbiased Extended Object Tracking”. In: *Proceedings of the 18th International Conference on Information Fusion (Fusion 2015)*. Washington D.C., USA, July 2015.

[25] Tim Baur, Patrick Hoher, Johannes Reuter, and Uwe D. Hanebeck. “Tracking Extended Objects with Basic Parametric Shapes Using Deformable Superellipses”. In: *Proceedings of the 27th International Conference on Information Fusion (Fusion 2024)*. Venice, Italy, July 2024.

[26] Charles Dugas, Yoshua Bengio, François Bélisle, Claude Nadeau, and René Garcia. “Incorporating second-order functional knowledge for better option pricing”. In: *Advances in neural information processing systems (NeurIPS)* 13 (2000).

[27] Antonio Zea, Florian Faion, and Uwe D. Hanebeck. “Exploiting Clutter: Negative Information for Enhanced Extended Object Tracking”. In: *Proceedings of the 18th International Conference on Information Fusion (Fusion 2015)*. Washington D.C., USA, July 2015.